J Mater Sci (2012) 47:824–832
DOI 10.1007/s10853-011-5860-6

Interfacial nature of Ag nanoparticles supported on TiO_2 photocatalysts

Jun-Gill Kang · Youngku Sohn

Received: 5 May 2011 / Accepted: 8 August 2011 / Published online: 24 August 2011

Abstract Silver nanoparticles supported on anatase TiO_2 nanoparticles have been prepared by deposition–precipitation, and characterized by X-ray photoelectron spectroscopy, including scanning electron microscopy, X-ray diffraction crystallography, Raman, and UV–visible absorption spectroscopy. The Ag 3*d* peak and the X-ray diffraction patterns show characteristics of purely metallic Ag, with no indication of Ag oxide species. Depth-profiling X-ray photoelectron spectroscopy with Ar^+ ion beam sputtering show a significant change in Ti 2*p*, and an asymmetric broadening of Ag 3*d* to a higher binding energy side. A decrease in major Ti $2p_{3/2}$ at 459.2 eV and a significant increase in lower binding energy peak are due to change in oxidation state of Ti from +4 to +3/+2. A broadening of Ag 3*d* peak with sputtering time is tentatively assigned to a final state quantum size effect. Upon annealing the deposition–precipitation sample, no significant change in Ag 3*d* peak is observed, while Ti 2*p* and O 1*s* XPS intensities are reduced, plausibly due to change in analyzed surface area for TiO_2. The photocatalytic activity for the photodegradation of methyl orange is dramatically reduced upon high Ag-loading, compared to bare TiO_2. The X-ray photoelectron spectroscopy of Ag on TiO_2 prepared by an electrochemical deposition reveals that Ag is also metallic, with no evidence of an oxide form. Upon annealing the electrodeposited sample, the Ag 3*d* peak shifts by +0.3 eV, while the Ti 2*p* and O 1*s* show no critical change in intensity and peak position.

J.-G. Kang
Department of Chemistry, Chungnam National University, Daejeon 304-764, Korea

Y. Sohn (✉)
Department of Chemistry, Yeungnam University, Gyeongsan, Gyeongbuk 712-749, Korea
e-mail: youngkusohn@ynu.ac.kr

Introduction

Titanium dioxide (TiO_2) has explosively been studied as a good model material for solar cell, water splitting, and photocatalysts, and widely applied in various fields [1–5]. Nowadays, to achieve a material of a more enhanced performance, impregnation of guest elements into transition metal oxides and surface modification of the oxides have actively been under performance [2, 6–12]. Enache et al. [8] used TiO_2 as a support for Au/Pd catalyst, and found very efficient turnover frequencies for the oxidation of alcohols. Park et al. [9] prepared carbon-doped TiO_2 nanotube arrays, and showed enhanced water splitting under visible-light absorption. Zhang and He [10] also used TiO_2 as a support for Pt catalyst, and found a complete oxidization of HCHO at room temperature. Kim et al. [11] fabricated a double (undoped TiO_2 and Cr-doped TiO_2) layer solar cell, and achieved an improved efficiency, compared to that of TiO_2 single layer. Gao et al. [12] tested photodegradation of bisphenol A using Zr-doped TiO_2 catalyst, and found a much higher photoactivity than undoped TiO_2. Chen et al. [6] modified the surface of white TiO_2 through hydrogen, and obtained black hydrogenated TiO_2, which showed substantial photocatalytic activities.

Ag, as a guest has also been introduced into (or onto) TiO_2 using various methods including sol–gel, solvothermal, hydrothermal, and photo-reduction methods, and widely applied to antibacterial- and photo-catalysts [13–33]. Guin et al. [24] prepared Ag on TiO_2 by a photo-reduction method in Ag nitrate–TiO_2 mixed solution, and tested antibacterial activities. Yu et al. [32] prepared Ag–TiO_2 composite by a sol–gel method, and found an enhanced bactericidal activity, compared to bare TiO_2. Yu et al. [22] tested photo-decolorization of methyl orange

using Ag–TiO_2 catalyst, and found 6.3-fold increase in efficiency, compared to bare TiO_2. In addition to those applications, photochromic effect of Ag–TiO_2 has been applied to multicolor systems [34–37].

In this article, being motivated by the reported studies, we have modified the surface of TiO_2 with Ag using precipitation-deposition (DP) and electrochemical deposition methods, and fully characterize the interfacial electronic structures by X-ray photoelectron spectroscopy (XPS). Valence band spectra taken by XPS are also included in this article although more detailed valence band structures are commonly obtained by ultraviolet photoelectron spectroscopy. Understanding valence band is very important because chemical reaction, bonding, electron (or hole) transfer processes, and wave-function mixing between two materials are mainly determined by the electronic structures [38]. In addition, because valence band is influenced by size, morphology, and the supports, by changing theirs we could tailor the properties of a system.

Experimental

We used anatase TiO_2 nanopowder (99.7%, <25 nm in size) purchased from Aldrich. For the impregnation of Ag, 0.1 M Ag nitrate solution (Yakuri Pure Chemical Co., LTD) was added into a TiO_2-dispersed water solution at 70 °C, followed by adding ammonia and glucose. This silver reduction is commonly known as silver mirror reaction (Tollen's test). Upon addition, we observed a change in color from white to dark, and kept stirring until no further change in color was observed. The final products was washed, and dried in an oven at 60 °C. For the electrochemical deposition of Ag, we first coated TiO_2 on a Si substrate, and completely dried at 100 °C. Ag was then electrodeposited on the substrate (2.5 mm × 15 mm) in a conventional three-electrode cell (CH Instruments) with a Ag/AgCl and a Pt wire electrodes for a reference and counter, respectively. Ag was electrodeposited on the TiO_2 potentiostatically by amperometry in an electrolyte solution mixed with 1 mM Ag (II) perchlorate hydrate (98%, Aldrich) and 0.1 M $NaClO_4$.

The prepared Ag–TiO_2 samples were imaged by SEM (Hitachi, SE-4800) combined with energy dispersive X-ray (EDX) elemental analysis. For UV–visible absorption spectra, we used Perkin-Elmer Lamda 35 equipped with Lapshere. For Raman spectra, we utilized Bruker Senterra confocal microscope at a laser excitation of 532 nm (a courtesy of professor K. T. Leung, University of Waterloo, Canada, www. watlab.com). The X-ray diffraction (XRD) of Ag–TiO_2 powder sample was taken using a PANalytical X'Pert Pro MPD diffractometer with Cu Kα radiation. The Ar^+ ion depth-profiling XPS was performed using a Thermo-VG Scientific MultiLab 2000 with an Al *Kα* X-ray source (1486.6 eV), a pass energy of 20.0 eV, and a hemispherical energy analyzer. No critical surface charging during the XPS measurements was observed; thereby, no correction of binding energy was performed.

Results and discussion

Figure 1 shows the SEM images of as-prepared precipitation–deposition (DP) and electrodeposited Ag nanoparticles (NPs) on TiO_2 supports. Ag NPs (~ 10 nm) are clearly discriminated from the TiO_2 support, and uniformly distributed on the support. For electrodeposited sample, Ag NPs distribute mainly on the topmost surface, while for DP sample Ag NPs uniformly distribute inside the bulk as well as the surface, as expected. The Ag deposition was also confirmed by an EDX (not shown) analysis. For the SEM image of the 450 °C-annealed DP sample, it appears that the Ag NPs become aggregated to form a larger Ag island. The as-prepared and annealed Ag NPs dispersed in water show a slight difference in photo color, indicating a change in particle size upon annealing.

The XRD patterns of the as-prepared and 450 °C-annealed Ag on TiO_2 are displayed in Fig. 2. The patterns are assigned to tetragonal anatase TiO_2 (JCPDS 21-1272) with (101), (004), (200), (105), (211), (204), and (220) planes [39], and cubic metallic Ag (JCPDS 41-1402) with (200), (111), and (220) planes [40, 41]. No peaks corresponding to Ag oxides were found. A formation of metallic Ag during DP could also be judged by change in color, and tiny silver mirror formation inside the wall of the reaction flask. Upon annealing to 450 °C, the major XRD patterns show no critical change, but the peak becomes a bit narrower, indicating formation of a larger island. This is in good consistency with the SEM image in Fig. 1. We have also induced sonication during DP. The XRD is displayed below in Fig. 2 for reference. Based on the SEM image (not shown) and the sharper XRD patterns, it appears that Ag forms larger islands. We have also simply tested photochromism of our sample [37] although this is not a main focus in this article. Upon irradiation of UV light for 30 min, we clearly observed a change in color (not shown) of the Ag–TiO_2 film by eye.

We have taken UV–Vis absorption and Raman spectra for further references, displayed in Fig. 3. As seen in the Figure, upon Ag-modification the absorption in the visible region is clearly enhanced due to nano-size metallic Ag. Compared to the 450 °C-annealed and the sonication-induced samples, the as-prepared sample shows an enhanced absorption in the visible region, plausibly due to a morphology (e.g., size) effect. Four Raman active peaks are observed between 100 and 900 cm^{-1}, attributed to

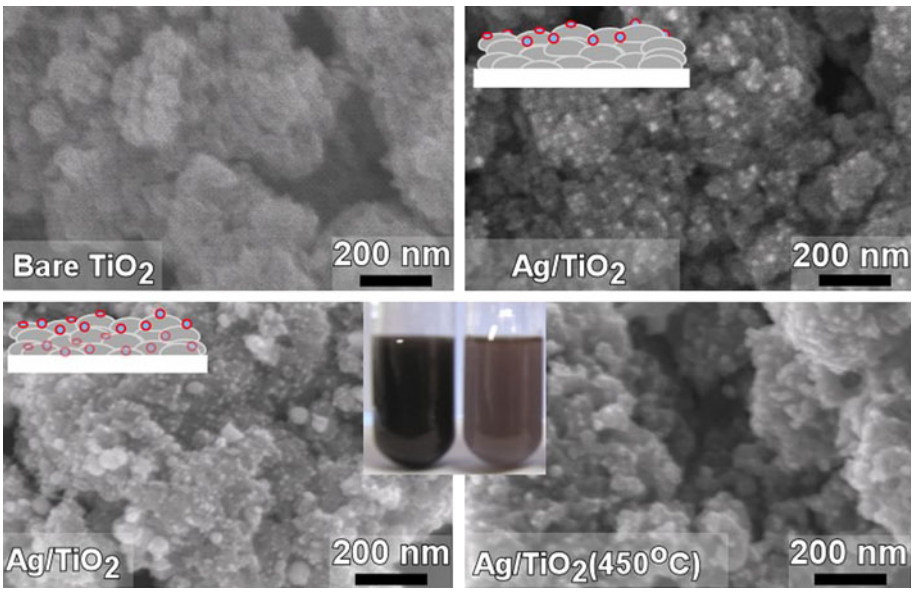

Fig. 1 SEM images of bare TiO_2 (*top left*), electrodeposited (*top right*), as-prepared DP (*bottom left*), and 450 °C-annealed (*bottom right*) Ag on TiO_2 supports. The *inset* photo images correspond to as-prepared and 450 °C-annealed DP samples dispersed in water

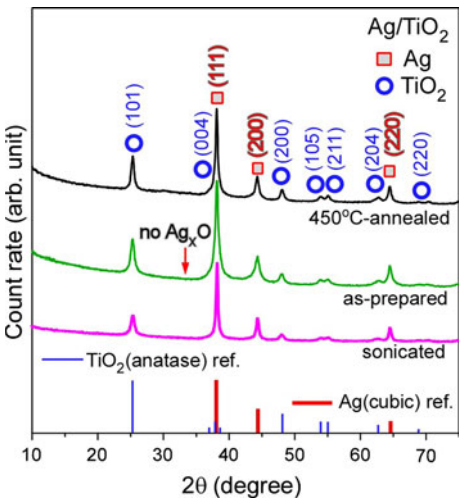

Fig. 2 XRD patterns of as-prepared and 450 °C-annealed DP Ag on TiO_2 nanoparticle support. Anatase TiO_2 and cubic metallic Ag XRD patterns are displayed below for reference. The XRD of a sonication-induced sample during DP is displayed for reference

anatase TiO_2 [42]. The peaks at 144 (E_g) and 394 cm^{-1} (B_{1g}) are of O–Ti–O bending. The other two peaks at 514 (A_{1g}) and 636 cm^{-1} (E_g) are due to Ti–O stretching. Upon high loading Ag, the Raman peaks are drastically reduced. This indicates that TiO_2 is almost fully covered by Ag. Upon annealing to 450 °C, the peak is further reduced to show no peaks. This could indicate Ag becomes more homogeneous than the as-prepared film. For the sonication-induced sample, the Raman peak of TiO_2 is still seen, indicative of lower coverage. As shown, the UV–visible absorption intensity in the visible region, and the relative XRD intensities of Ag/TiO_2 is lower, compared to the other two samples.

We performed depth profiling XPS to further clarify changes in chemical states and electronic structures with depth. Figure 4 shows the XPS survey and high resolution narrow scans. The major XPS survey peaks include O 1*s*, Ti 2*p*, Ag 3*d*, and C 1*s*. The C 1*s* XPS peak due to surface impurity is significantly decreased upon sputtering as expected. Other XPS peaks show no comparable change in intensity, relatively compared to the C 1*s* peak. The high resolution Ag 3*d* peaks for the as-prepared sample are located at 368.0 eV ($3d_{5/2}$) and 374.0 eV ($3d_{3/2}$), with a spin–orbit splitting of 6.0 eV. This is attributed to metallic Ag [42], consistent with the XRD result. The Ti $2p_{3/2}$ ($2p_{1/2}$) peak is found at 459.3 (465.1) eV, attributed to Ti^{4+} of bulk TiO_2 [39]. The peak position and width show no critical change compared to those of unmodified bare TiO_2. This indicates that there is no significant interfacial interaction between Ag and the support. Upon Ag deposition, the O 1*s* peak at ~533.0 eV is enhanced, as clearly shown from the difference spectrum (O 1*s* Ag/TiO_2–O 1*s* bare TiO_2). The enhanced peak is plausibly due to weakly adsorbed species such as H_2O (and/or O_2). The major peak at 530.5 eV is due to O^{2-} of TiO_2 [39]. The valance band (VB) shows a broad distribution between 2 and 10 eV, due to both Ag 4*d*, and π-nonbonding/σ-bonding O 2*p* orbitals for TiO_2 [39]. To discriminate net Ag 4*d* signal from the TiO_2 support, we take a difference VB spectrum (Ag/TiO_2–bare TiO_2), and attribute this solely to Ag $4d_{5/2,3/2}$ VB. With sputtering the surface, the Ag 3*d* peak shifts slightly to a higher BE position by only 0.1 eV (within experimental uncertainty), and becomes asymmetrically broadened toward higher BE side. Upon 10 min sputtering, the Ag 3*d* peak is enhanced by 1.1×. The normalization factor is then 0.93 for the 10 min-sputtered Ag 3*d* peak. The enhancement could be due to removal of surface carbon

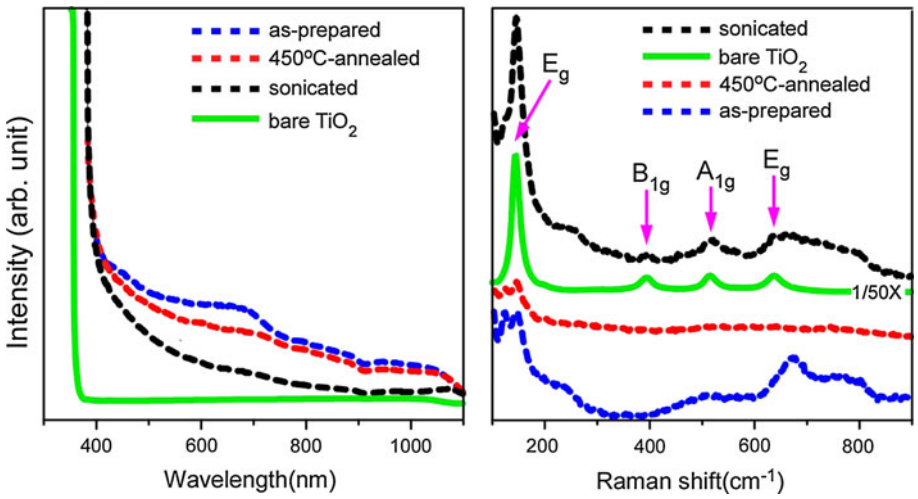

Fig. 3 UV–visible absorption (*left*) and Raman (*right*) spectra of bare TiO_2 (*green*), as-prepared (*blue*), 450 °C-annealed (*red*), and sonication-induced (*black*) DP Ag on TiO_2. The Raman spectrum of bare TiO_2 is scaled by 1/50× (Color figure online)

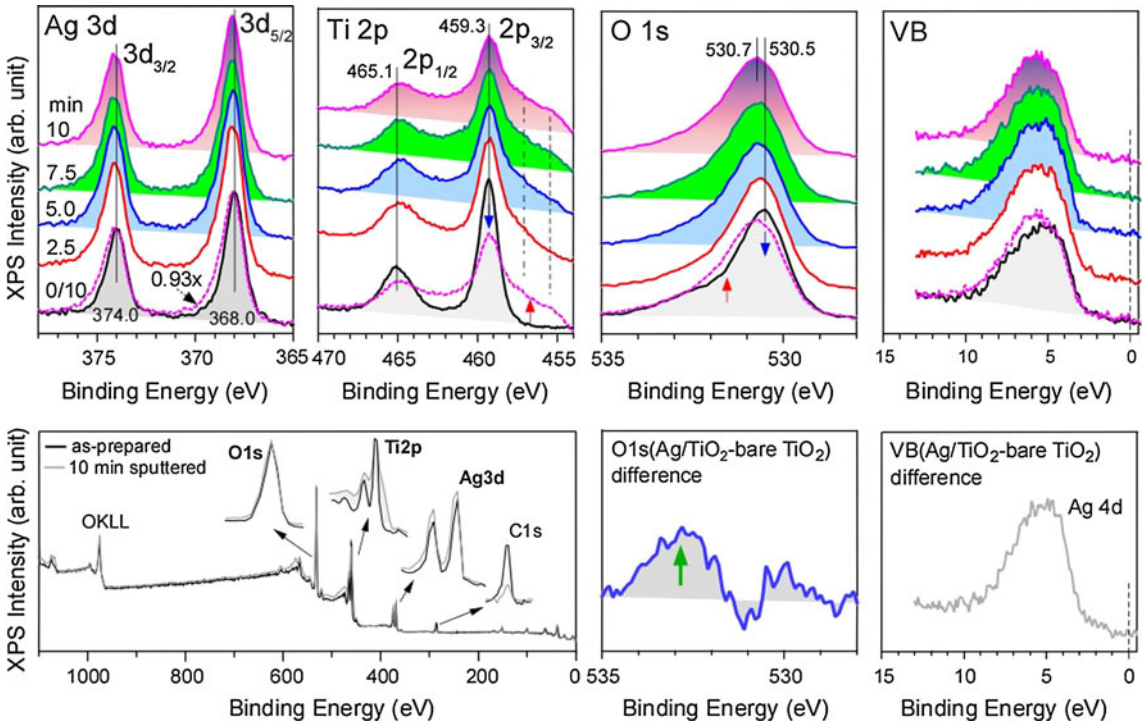

Fig. 4 High resolution Ag 3*d*, Ti 2*p*, O 1*s*, and VB XPS spectra (*top*) with sputtering time, and survey XPS spectra (*bottom left*) of as-prepared DP Ag on TiO_2. 0/10 indicates 0 and 10 min spectra display at the same baseline

contaminants. The asymmetrical broadening is due to either initial or final state effects [44, 45]. A final state charging effect is plausibly considered. When the size of a Ag NP reaches to a quantum size by sputtering the positive charge inside the NP become isolated from the substrate [44]. Thereby, the XPS peak is observed in a higher BE side. The Ti 2*p* XPS peak drastically changes with sputtering. The Ti $2p_{3/2}$ peak at 459.3 eV becomes reduced while the peak in the lower BE side becomes remarkably enhanced. This has been attributed to lower oxidation states of Ti (Ti^{n+}, $n < 4$) induced by ion beam irradiation [39]. For the O 1*s* XPS peak with sputtering, the peak maximum slightly shifts to a higher BE position from 530.5 to 530.7 eV. The photoemission intensity at 530.5 eV is reduced while that at 531.5 is enhanced. The change in total O 1*s* intensity is negligibly small, indicating no loss of oxygen by sputtering. The O 1*s* peak at ~531.5 eV is attributed to defects and/or adsorbed OH. It has been reported that OH species could be formed by ion beam irradiation [39, 46]. Furthermore, defects are also created when Ti^{3+} and Ti^{2+} are formed by reduction of Ti^{4+}. The VB spectra broaden toward a higher BE side with

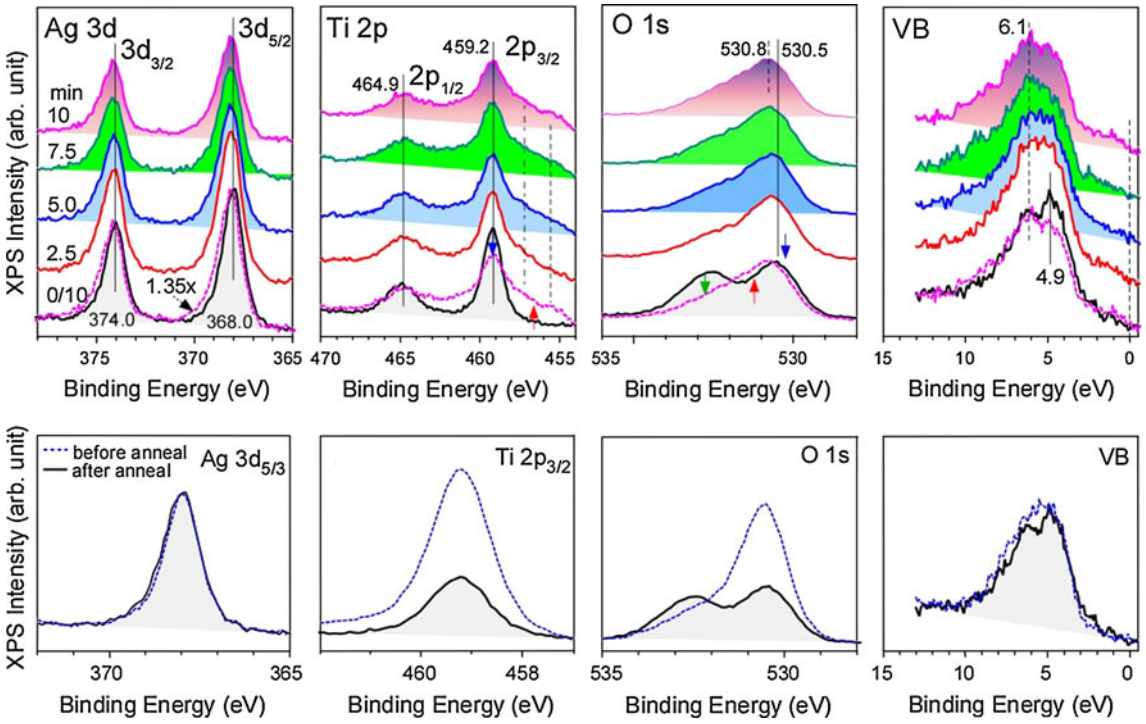

Fig. 5 High resolution Ag 3*d*, Ti 2*p*, O 1*s*, and VB XPS spectra (*top*) of 450 °C-annealed DP Ag on TiO_2 with sputtering time. 0/10 indicates 0 and 10 min spectra display at the same baseline. The Ag 3*d*, Ti 2*p*, O 1*s* and VB XPS spectra of as-prepared and annealed samples display at the same baseline

increasing sputtering, due to mostly change in chemical state of TiO_2.

Upon annealing the DP sample, the XPS spectra show differences as displayed in Fig. 5. The Ti 2*p* and O 1*s* spectra remarkably change, while the Ag 3*d* spectrum shows no significant change. The enhanced O 1*s* peak at 532.5 eV is due to an increase in weakly adsorbed oxygen species such as H_2O and O_2. The major Ti 2*p* and O 1*s* peak are reduced in intensity with no change in BEs. This reflects that the analyzed surface area of TiO_2 is decreased upon annealing. As discussed above (Fig. 1), the morphology of DP sample changes considerably upon annealing. The Ag 3*d* peak is gradually decreased with sputtering. The intensity is reduced by 0.74×, and thus the normalization factor is 1.35×. An asymmetric broadening of the Ag 3*d* peak to a higher BE side is plausibly due to a quantum size effect, as already discussed above. The Ti 2*p* peak changes very similarly to that of unannealed DP sample. The Ti 2*p* (Ti^{4+}) peak at 459.2 eV is reduced while the Ti 2*p* (Ti^{n+}, $n < 4$) peak with a lower BE is enhanced due to an ion beam sputtering effect, as discussed above. The O 1*s* XPS peak at 532.5 eV is dramatically reduced upon 2.5 min sputtering, reflecting removal of topmost adsorbed species. Upon further sputtering, the O 1*s* peak changes very similarly to that (Fig. 5) of unannealed DP sample. Two VB maxima appear at 4.9 and 6.1 eV, and resemble that of metallic Ag [19]. With increasing sputtering, the VB becomes blunt plausibly due to size effect and/or change in chemical states of TiO_2 support. We have roughly calculated the relative elemental surface composition of Ag versus Ti for the DP sample, assuming that the Ag and TiO_2 are homogeneously mixed. The XPS peaks of Ag 3*d* and Ti 2*p* were integrated, and divided the areas by their corresponding sensitivity factors (Ti 2*p* = 1.9 and Ag 3*d* = 5.2) [47]. Then, the Ag/Ti ratios were calculated to be 1/7.5 ≈0.13 and 1/2.7 ≈0.37 for the as-prepared and the annealed samples, respectively. The difference in ratio is mainly due to decrease in Ti 2*p* intensity upon annealing, already discussed above.

Photocatalytic activities of DP samples were tested for the photodegradation of methyl orange. The degradations catalyzed by unmodified TiO_2 and Ag-modified TiO_2 powders (un-annealed and 450 °C-annealed) are displayed with UV (365 nm) irradiation time. The UV–Vis spectra of methyl orange solution containing bare TiO_2 are displayed with photo-irradiation time for reference. As seen in Fig. 6, without a catalyst the absorption maximum (λ_{max}) shows no change with time. Upon adding anatase to TiO_2 nano-powders, the degradation of methyl orange drastically occurs with photo-irradiation time. For Ag-modified TiO_2, the degradation rate becomes remarkably slower. And the rates for the as-prepared and 450 °C-annealed DP samples show no considerable change. As discussed above, the chemical states of Ag and TiO_2 elucidated by XPS show no

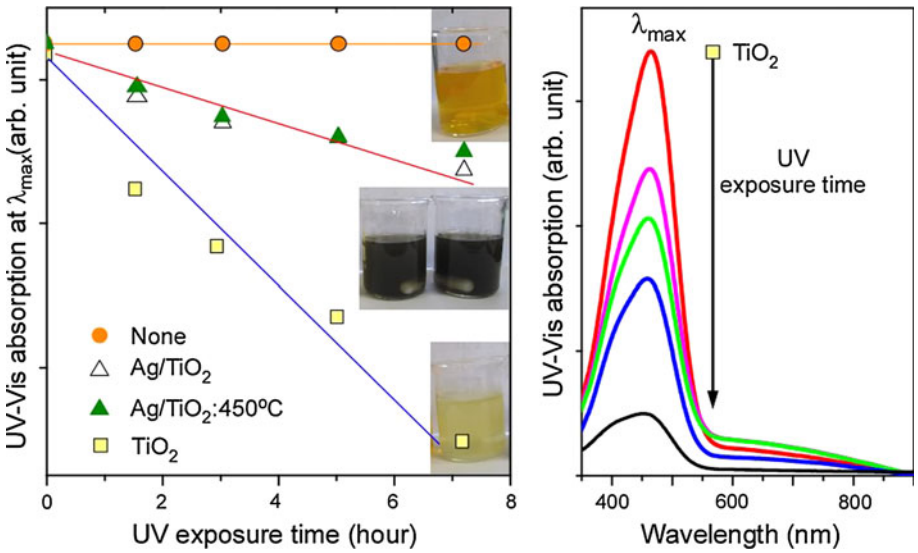

Fig. 6 Photodegradation of methyl orange with UV (365 nm) exposure time, and the UV–Vis absorption spectra for TiO_2 photocatalyst with increasing UV exposure time

critical change. It appears that the lower degradation rate could be due to a high Ag-loading effect. It has commonly been observed that the best efficiency is obtained at a low loading level [47–50]. Moon et al. [48] doped Sb into TiO_2 to increase photocatalytic activity, found a better activity than that of Degussa P-25 for the photodecomposition of methylene blue at 5% doping level. At above 5%, they found that the activity becomes deteriorated. Sano et al. [49] photodeposited Ag on TiO_2, and obtained the best efficiency at 0.16 wt% Ag for the photodecomposition of N_2O. They attributed the increased efficiency to Ag^+ species. Dobosz and Sobczynski obtained the optimum condition at 0.5 wt% Ag in TiO_2 for phenol decomposition, and found a decrease in decomposition efficiency at above the Ag loading level [51] .

We have compared the XPS of DP sample with that of electrodeposited sample. For Ag on TiO_2 prepared by electrodeposition, the corresponding XPS spectra are displayed in Figs. 7 and 8. The survey XPS scan also includes Ag 3*d*, Ti 2*p*, O 1*s*, and C 1*s* (surface impurity), as expected. The Ag $3d_{5/2}$ ($3d_{3/2}$) peak is found at 368.1 (374.1) eV, assigned to metallic Ag. The Ag 3*d* peak becomes also asymmetrically broadened toward a higher BE side with increasing sputtering time. The intensity is reduced by 0.5×, and then the normalization factor is 2×. The Ag 3*d* XPS intensity is more drastically reduced with sputtering, compared to the DP sample. This is because as mentioned earlier Ag NPs mainly exist on the topmost surface for an electrodeposited sample, not inside the bulk. The Ti $2p_{3/2}$ ($2p_{1/2}$) peak at 459.2 (465.0 eV) is the same as that of bare TiO_2, indicating no critical interfacial interactions between Ag and the support. With increasing ion beam sputtering, the major Ti 2*p* peak becomes reduced while the lower BE peak is enhanced. This change is very similar to that for DP sample. Upon Ag deposition, the O 1*s* XPS peak between 531 and 534 eV is enhanced while the major peak at 530.6 eV is reduced. With increasing sputtering, the photoemission between 531 and 535 eV are increased due to enhancement of adsorbed H_2O (and O_2, OH) and defects [39]. On the other hand, the major peak is consequently reduced. The VB also changes very similarly as that of DP sample. The difference (Ag/TiO_2–bare TiO_2) VB spectrum is attributed to entirely overlayer Ag 4*d*. With sputtering, the VB becomes broadened, and the maximum shifts from 5.2 to 6.6 eV.

For 450 °C-annealed electrodeposited sample, the Ag 3*d* and VB changes significantly, while the Ti 2*p* and O 1*s* show a very little change, compared to the unannealed sample. The BE of Ag 3*d* shifts to a higher BE by 0.3 eV, and the VB maximum shifts by 1.5 eV. The Ag 3*d* peak shift is not due to a change in oxidation state, plausibly due to a support electronic effect. Emphasized here that, in XPS the Ag 3*d* BE of Ag oxides is lower than that of metallic Ag. The Ti 2*p* and O 1*s* XPS peaks shift merely by 0.1 eV, with no critical change in intensity. The O 1*s* peak upon annealing shows a slight decrease at ~531.5 eV and a slight increase at ~533 eV, indicating a small change in oxygen chemical states.

Now here, we should discuss that the oxidation state of Ag may also play a significant role in a photocatalytic activity. In other words, it is important to know chemical states of Ag for better understanding photocatalytic properties. Table 1 summarizes the XPS-probed chemical states of Ag on TiO_2 support prepared by various methods reported in literatures. It has commonly been observed that Ag is metallic for samples prepared by DP and photoreduction methods. Ag oxides are generally formed by UV or thermal treatments after preparing by a sol–gel process. A thermal-treated (200–300 °C) Ag prepared by a photoreduction method was also shown to be an oxide form. As

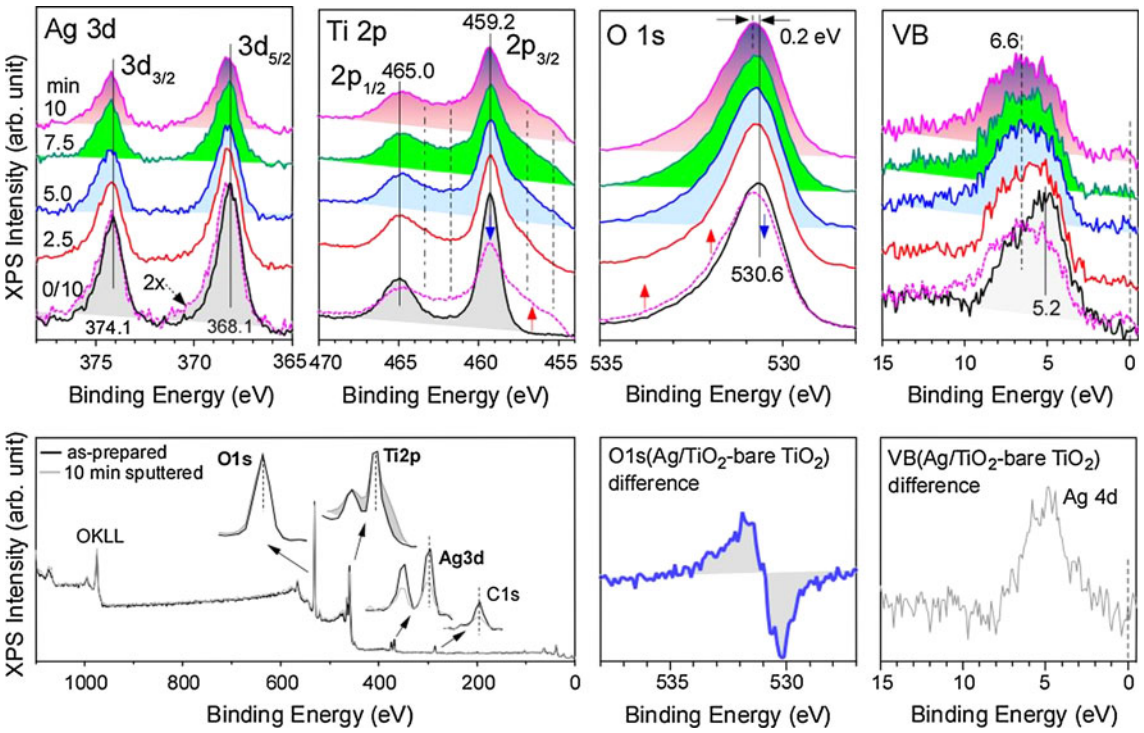

Fig. 7 High resolution Ag 3*d*, Ti 2*p*, O 1*s*, and VB XPS spectra (*top*) with sputtering time, and survey XPS spectra (*bottom left*) of electrodeposited Ag on TiO_2. 0/10 indicates 0 and 10 min spectra display at the same baseline

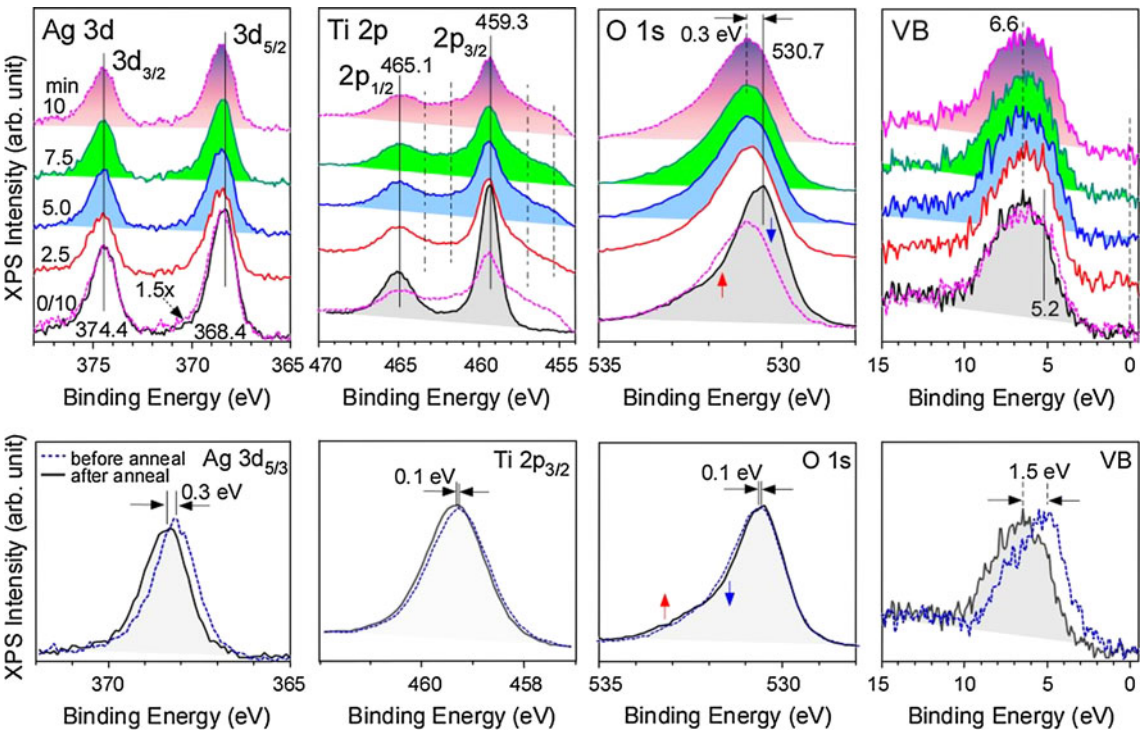

Fig. 8 High resolution Ag 3*d*, Ti 2*p*, O 1*s*, and VB XPS spectra (*top*) of 450 °C-annealed electrodeposited Ag on TiO_2 with sputtering time. 0/10 indicates 0 and 10 min spectra display at the same baseline. The Ag 3*d*, Ti 2*p*, O 1*s*, and VB XPS spectra of as-prepared and annealed samples display at the same baseline

Table 1 A literature review for chemical states (XPS BE) of Ag on TiO_2 prepared by various methods

Preparation methods	Ag chemical states in $3d_{5/2}$ ($3d_{3/2}$), eV		XPS instruments, [Reference no.]
	Metallic	Oxide form	
DP method (chemical deposition)	368.0 (374.0): as prep. and anneal	None	MultiLab 2000, this study
	368.1 (374.1): as prep. and anneal	None	ESCALab 250 [29]
	368.5 (374.5)	None	PHI 5000C ESCA [52], Escalab M K_{11} [53]
Electrodeposition	368.1 (374.1): as prep.	None	MultiLab 2000, this study
	368.4 (374.4): anneal		
Liquid phase deposition	368.0 (374.0)	None	[22]
Sol–gel method	368.5: as prep.	None	Kratos Axis Ultra spectrometer [32]
	After UV exposure: Ag_2O (367.9 eV) and Ag^0 (368.6 eV)		
	450 °C anneal 368.2 (374.2)	None	PHI Quantum 2000 [61]
	400 °C anneal: Ag^0 (368.2), AgO (367.0 eV), and Ag_2O (367.7 eV),		Escalab MK II [54]
	500 °C anneal-anatase	800°C anneal-rutile	ESCA 2000 [60]
	368.2 and 374.5	Ag_2O, ~ 367.5 eV	
	368.4 (as-prep.)	None	Perkin-Elmer Φ 5600ci [27]
	Anneal: 367.9–368.3 eV: Ag(0) → Ag(I)		
	368.6 (375.8)	None	[24]
	None	Ag_2O: 367.8 (373.6)	[62]
Ag deposition (RF method) on xerogel	368.5 (375.5)	None	[25]
Photo-reduction method	368.1 (374.1)	None	ESCALab220i-XL [55]
	367.6 (373.5 ± 0.1)	None	PHI 5600 [56, 58]
	367.2 (373.2):charge transfer interaction	None	PHI 5000C ESCA [57]
	300 °C anneal		Thermo VG [59]
	(Ag^0, 368.2): minor/(Ag_2O, 367.8): major		
	368.2: as-prep., and	367.6 (Ag_2O):	PE PHI Quantera
	450 °C anneal	200 °C anneal	SXM [63]

mentioned, different oxidation states of Ag are prepared by changing the preparation methods. Thereby, different photocatalytic activities are achieved at low Ag concentration levels. Using our experimental setup, we could not really measure a change in photocatalytic activity for the electrodeposited sample because the surface area of the sample is only 2.5 mm × 15 mm. For a direct comparison of photocatalytic activities between DP and electrodeposited samples, we consider it as a future plan.

Summary

Efficient Ag deposition on TiO_2 support has been performed by deposition–precipitation (DP) and electrochemical deposition methods. Ag 3*d* XPS peaks and XRD patterns are of purely metallic Ag. With increasing Ar^+ ion beam sputtering, Ag 3*d* XPS peak becomes asymmetrically broadened to a higher BE side. This is attributed to a final state quantum size effect. Ti 2*p* XPS peak significantly changes with increasing sputtering, due to change in oxidation state of Ti from 4+ to lower oxidation states (3+ and 2+). Photocatalytic activity of bare TiO_2 for methyl orange degradation becomes deactivated upon high Ag-loading. Our study further deepens interfacial nature of Ag and a metal oxide support for understanding the origin of catalytic active or inactive sites.

Acknowledgements This research was supported by the Yeungnam University research grants in 2009.

References

1. Kudo A, Miseki Y (2009) Chem Soc Rev 38:253
2. Fujishima A, Zhang X, Tryk DA (2008) Surf Sci Rep 63:515
3. Macwan DP, Dave PN, Chaturvedi S (2011) J Mater Sci 46:3669. doi:10.1007/s10853-011-5378-y
4. Ni M, Leung MKH, Leung DYC, Sumathy K (2007) Renew Sust Energy Rev 11:40
5. Zou J, Zhang Q, Huang K, Marzari N (2010) J Phys Chem C 114:10725
6. Chen X, Liu L, Yu PY, Mao SS (2011) Science 331:746
7. Khan SUM, Al-Shahry M, Ingler W B Jr (2002) Science 297:2243

8. Enache DI, Edwards JK, Landon P, Solsona-Espriu B, Carley AF, Herzing AA, Watanabe M, Kiely CJ, Knight DW, Hutchings GJ (2006) Science 311:362
9. Park JH, Kim S, Bard AJ (2006) Nano Lett 6:24
10. Zhang C, He H (2007) Catal Today 126:345
11. Kim C, Kim KS, Kim HY, Han YS (2008) J Mater Chem 18:5809
12. Gao B, Lim TM, Subagio DP, Lim TT (2010) Appl Catal A 375:107
13. Lassaletta G, Gonzalez-Elipe AR, Justo A, Fernandez A, Ager FJ, Respaldiza MA, Soares JC, Da Silva MF (1996) J Mater Sci 31:2325. doi:10.1007/BF01152941
14. Yang C, Liang GL, Xu KM, Gao P, Xu B (2009) J Mater Sci 44:1894. doi:10.1007/s10853-009-3247-8
15. Li Y, Ma M, Chen W, Li L, Zen M (2011) Mater Chem Phys 129:501
16. Pastoriza-Santos I, Koktysh DS, Mamedov AA, Giersig M, Kotov NA, Liz-Marzan LM (2000) Langmuir 16:2731-1
17. Lange de Oliveira A, Wolf A, Schuth F (2001) Catal Lett 73:157
18. Sokmen M, Candan F, Sumer Z (2001) J Photochem Photobiol A 143:241
19. Gruenert W, Brueckner A, Hofmeister H, Claus P (2004) J Phys Chem B 108:5709
20. Hirakawa T, Kamat PV (2005) J Am Chem Soc 127:3928
21. Chan SC, Barteau MA (2005) Langmuir 21:5588
22. Yu J, Xiong J, Cheng B, Liu S (2005) Appl Catal B 60:211
23. Zhang F, Pi Y, Cui J, Yang Y, Zhang X, Guan N (2007) J Phys Chem C 111:3756
24. Guin D, Manorama SV, Latha JNL, Singh S (2007) J Phys Chem C 111:13393
25. Akhavan O (2009) J Colloid Interface Sci 336:117
26. Zhang H, Chen G, Bahnemann DW (2009) J Mater Chem 19:5089
27. Armelao L, Barreca D, Bottaro G, Gasparotto A, Maccato C, Tondello E, Lebedev OI, Turner S, Van Tendeloo G, Sada C, Lavrencic Stangar U (2009) ChemPhysChem 10:3249
28. Sangpour P, Hashemi F, Moshfegh AZ (2010) J Phys Chem C 114:13955
29. Mai L, Wang D, Zhang S, Xie Y, Huang C, Zhang Z (2010) Appl Surf Sci 257:974
30. He X, Cai Y, Zhang H, Liang C (2011) J Mater Chem 21:475
31. Song C, Wang D, Xu Y, Hu Z (2011) Mater Lett 65:908
32. Yu B, Leung KM, Guo Q, Lau WM, Yang J (2011) Nanotechnology 22:115603
33. Dunnill CW, Page K, Aiken ZA, Noimark S, Hyett G, Kafizas A, Pratten J, Wilson M, Parkin IP (2011) J Photochem Photobiol A 220:113
34. Preclikova J, Galar P, Zidek K, Trojanek F, Maly P (2010) J Nanosci Nanotechol 10:2630
35. Han R, Zhang X, Wang L, Dai R, Liu Y (2011) Appl Phys Lett 98:221905/1
36. Matsubara K, Tatsuma T (2007) Adv Mater 19:2802
37. Naoi K, Ohko Y, Tatsuma T (2004) J Am Chem Soc 126:3664
38. Gomathi DL, Mohan RK (2011) Appl Surf Sci 257:6821
39. Sohn Y (2010) Appl Surf 257:1692
40. Patel AC, Li S, Wang C, Zhang W, Wei Y (2007) Chem Mater 19:1231
41. Sun Y, Xia Y (2002) Science 298:2176
42. Zhang WF, He YL, Zhang MS, Yin Z, Chen Q (2000) J Phys D 33:912
43. NIST, X-Ray Photoelectron Spectroscopy Database, NIST Standard Reference Database 20, Version 3.5 (Web version: http://srdata.nist.gov/xps/)
44. Sohn Y, Pradhan D, Radi A, Leung K T (2009) Langmuir 25:9557
45. Zhang P, Sham TK (2003) Phys Rev Lett 90:245502
46. Takeuchi M, Onozaki Y, Matsumura H, Uchida H, Kuji T (2003) Nucl Instrum Methods B 206:259
47. Briggs D, Seah MP (1990) Practical Surface Analysis Vol 1, 2nd edn. Wiley and Sons, Chichester
48. Moon J, Takagi H, Fujishiro Y, Awano M (2001) J Mater Sci 36:949. doi:10.1023/A:1004819706292
49. Sano T, Negishi N, Mas D, Takeuchi K (2000) J Catal 194:71
50. Dobosz A, Sobczynski A (2003) Water Res 37:1489
51. Tom RT, Nair AS, Navinder S, Aslam M, Nagendra CL, Philip R, Vijayamohanan K, Pradeep T (2003) Langmuir 19:3439
52. You X, Chen F, Zhang J, Anpo M (2005) Catal Lett 102:247
53. Du J, Zhang J, Liu Z, Han B, Jiang T, Huang Y (2006) Langmuir 22:1307
54. Xin B, Jing L, Ren Z, Wang B, Fu H (2005) J Phys Chem B 109:2805
55. Li H, Duan X, Liu G, Liu X (2008) J Mater Sci 43:1669. doi:10.1007/s10853-007-2387-y
56. Bansal A, Madhavi S, Tan TTY, Lim TM (2008) Catal Today 131:250
57. Li J, Xu J, Dai WL, Fan K (2009) J Phys Chem C 113:8343
58. Wodka D, Bielanska E, Socha RP, Elzbieciak-Wodka M, Gurgul J, Nowak P, Warszynski P, Kumakiri I (2010) ACS Appl Mater Interfaces 2:1945
59. Kuo YL, Chen HW, Ku Y (2007) Thin Solid Films 515:3461
60. Park MS, Kang M (2008) Mater Lett 62:183
61. Lai Y, Chen Y, Zhuang H, Lin C (2008) Mater Lett 62:3688
62. Page K, Palgrave RG, Parkin IP, Wilson M, Savin SLP, Chadwick AV (2007) J Mater Chem 17:95
63. Zhang H, Wang G, Chen D, Lv X, Li J (2008) Chem Mater 20:6543